CONCEPTUAL DESIGN OF THE MU2E PRODUCTION SOLENOID COLD MASS

V.V. Kashikhin[1], G. Ambrosio[1], N. Andreev[1], M. Lamm[1],
N.V. Mokhov[2], T.H. Nicol[1], T.M. Page[1], V. Pronskikh[2]

[1]TD, Fermilab, P.O. Box 500, Batavia, IL 60510 U.S.A.

[2]APC, Fermilab, P.O. Box 500, Batavia, IL 60510 U.S.A.

ABSTRACT

The Muon-to-Electron conversion experiment (Mu2e), under development at Fermilab, seeks to detect direct muon to electron conversion to provide evidence for a process violating muon and electron lepton number conservation that cannot be explained by the Standard Model of particle physics.

The required magnetic field is produced by a series of superconducting solenoids of various apertures and lengths. This paper describes the conceptual design of the 5 T, 4 m long solenoid cold mass with 1.67 m bore with the emphasis on the magnetic, radiation and thermal analyses.

KEYWORDS: Magnet, superconductor, solenoid.

INTRODUCTION

The Mu2e magnet system consists of three large superconducting solenoids [1]. The first in the chain of magnets is the Production Solenoid (PS). The role of the PS in Mu2e is to collect and focus pions, generated in interactions of an 8-GeV, 25 kW proton beam with the gold target, and muons from pion decays by supplying a peak axial field of 5 T and an axial field gradient of 1 T/m within a 1.5 m warm bore [2].

Because of the fixed target location inside of the magnet bore, PS is the most radiation-challenged magnet in Mu2e. Approximately 16 kW of the primary proton beam power goes to the particle radiation towards the superconducting coils. In order for the coils to operate reliably with a sufficient thermal margin, that number must be reduced by at least two orders of magnitude that is achieved by the heat and radiation shield (HRS).

The coils are installed inside of the support shells made of Al 5083-O and bolted together to form the cold mass assembly. The details related to the PS structural analysis, fabrication technology, powering and quench protection are discussed elsewhere [3].

The cold mass is suspended inside of the cryostat using a system of Inconel-718 rods reacting the forces due to gravity and electromagnetic interactions [4]. The cooling is by the thermal siphon scheme through the tubes installed on the outer cold mass surface.

CABLE AND INSULATION

In order to reduce the radiation heat load on the cryogenic system and increase the thermal margin, the conductor employs aluminum stabilizer placed around the Rutherford type cable by either conforming or hot extrusion. Such cable technology was used in nearly every large detector solenoid built in the past decades with the most recent examples being the ATLAS Central Solenoid, ATLAS Toroids and CMS [5]-[7].

The PS cable parameters are summarized in Table 1. A high-strength Al stabilizer is required to withstand the Lorentz forces during the magnet operation, while minimizing the cold mass thickness. The necessary stabilizer strength and RRR were achieved during the ATLAS R&D in the developed precipitation hardening Al-0.1wt%Ni alloy combined with the cold work [8]. This type of stabilizer material is the baseline choice for the PS cable.

Besides providing an adequate electrical strength and radiation resistance, the coil insulation should have a relatively high thermal conductivity to permit the heat extraction. The PS employs a composite cable insulation made of polyamide and pre-preg glass tapes.

TABLE 1. Cable parameters.

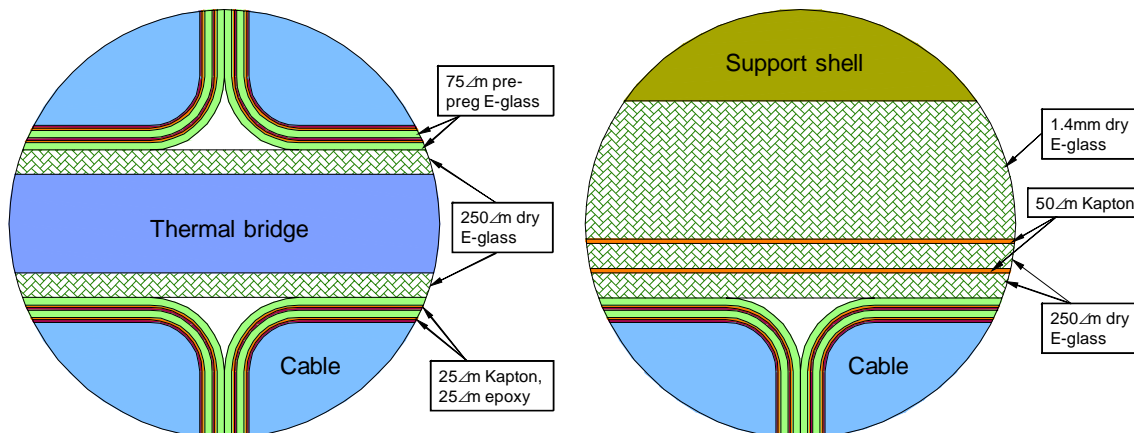| Parameter	Unit	Value
Rutherford cable		
Strand diameter	mm	1.300
Number of strands	-	36
Cable dimensions	mm^2	23.65 x 2.34
Critical current density at 5T, 4.2K	A/mm^2	>3000
Strand Cu/non-Cu ratio	-	0.9
Initial RRR of Cu matrix	-	>100
Al-stabilized cable		
Bare cable dimensions	mm	30.00 x 6.00
Overall stabilizer/superconductor ratio	-	6.16
Initial RRR of Al stabilizer	-	>500

FIGURE 1. Layouts of the cable/interlayer insulation (left) and ground insulation (right).

This type of insulation, originally developed for the TRISTAN/TOPAZ solenoid [9], was also used in the ATLAS Central Solenoid [10]. The cable is insulated with two layers of composite tape consisting of 25 μm of semi-dry epoxy on one side of 25 μm Kapton tape and 75 μm of pre-preg E-glass on the other side, as shown in Figure 1.

To facilitate the heat extraction from the coil and increase the structural integrity, all gaps between turns and layers are to be filled with epoxy resin during vacuum impregnation. Since the composite cable insulation is impermeable for epoxy, the sheets of dry E-glass insulation are introduced between the coil layers and between coil and support structure as shown in Figure 1 to provide paths for epoxy penetration. It will ensure a good thermal and structural contact between the cables, thermal bridges, and the support structure. The purpose and design of the thermal bridges as well as the ground insulation between the thermal bridges and the end flanges are discussed later in the text.

The ground insulation between the cables and the support structure with the total thickness of 2 mm consists of dry E-glass and 2x50 μm layers of Kapton, as shown in Figure 1. The extra thickness of E-glass between the coil and support structure provides allowance for possible machining of the outer coil surface after the impregnation.

MAGNETIC ANALYSIS

According to the requirements document [2], the PS magnet should have magnetic field gradient along the magnet axis with the peak field on the axis of >5 T and the field at the interface with the Transport Solenoid (TS) of ~2.5 T. It implies that the current per unit of length must vary by a factor of ~2 along the magnet.

In order to fulfill this requirement, the magnet consists of three 1.29 m long sections with a 4, 3 and 2 layers of cable wound in the hard way around the aperture. Figure 2 shows the magnet cross-section and the flux density diagram in the coil and yoke, and the flux density along the magnet axis. Note that the pictures also show the straight section of the TS that was included in the model for the field matching purposes.
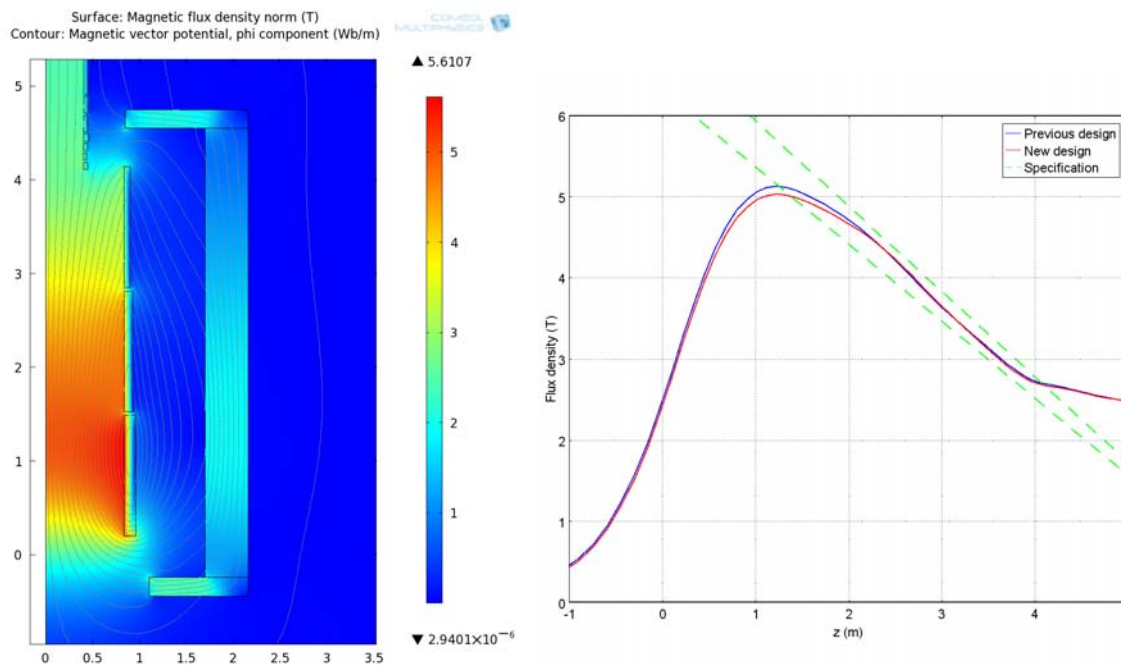

FIGURE 2. Magnet cross-section with the flux density diagram (left) and the axial field profile (right).

The field meets the requirements starting from the peak value of 5.0 T and down to 2.7 T at the beginning of TS. The peak field in the coil reaches 5.6 T in the first (upstream) coil, while the field in the yoke body is <2.0 T. The peak field in the end caps is ~2.4 T that is above the iron saturation point, but it poses no concern for the magnet design.

The magnet is designed to operate at 64.2 % of the Short Sample Limit (SSL) along the load line at the temperature of 4.6 K (no radiation heat load), as shown in Figure 3. At higher temperatures, the SSL shifts closer to the operating point and passes it at the temperature of 6.50 K - that is the current-sharing temperature at the operating current. In order to maintain the temperature margin requirement of 1.5 K at the operating current, the coil temperature shall not exceed 5.0 K. It is equivalent to operating at 68.9 % with respect to the SSL at 4.6 K. The main magnet parameters are summarized in Table 2.
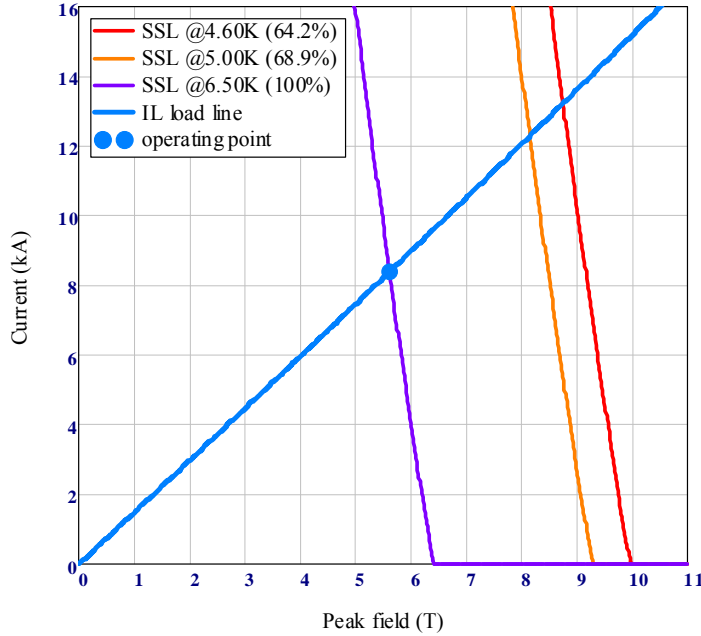

FIGURE 3. Magnet load line and short sample limits at different temperatures.

TABLE 2. PS magnet parameters.

Parameter	Unit	Value
Liquid helium temperature (T_{LHe})	K	4.60
Operating current (I_{op})	kA	8.40
Peak axial field at I_{op}	T	5.03
Peak coil field at I_{op}	T	5.61
Quench current at T_{LHe}	kA	13.23
Current sharing temperature at I_{op}	K	6.50
Minumum temperature margin	K	1.50
Maximum allowable temperature (T_{maxall})	K	5.00
Fraction of SSL at T_{LHe}		0.642
Fraction of SSL at T_{maxall}		0.689
Stored energy	MJ	77.33
Self-inductance	H	2.192
Cold mass inner diameter	m	1.67
Cold mass length	m	4.01
Cold mass weight	tonnes	11.8

RADIATION ANALYSIS

The radiation analysis was performed using MARS15 code [11]. The proton beam intensity was assumed $2 \cdot 10^{13}$ p/s, with the beam rms 0.1 cm hitting a 16 cm long 0.3 cm in diameter gold target. The exclusive model of secondary particle formation was used. The particle transport thresholds were 0.001 eV for neutrons, 1 MeV for muons and charged hadrons, 200 keV for γ-quanta, electrons and positrons.

The coil material was described in MARS15 as a homogeneous mixture of the elements comprising the coil, taken with proper weights. An extensive optimization of the HRS parameters was performed [**Error! Reference source not found.**]. Figure 4 shows the MARS15 model cross-section of the optimized HRS. The peak radiation quantities calculated inside of the coil, such as the absorbed dose, power density, dynamic heat load and DPA (displacement per atom) rate, summarized in Table 3, are within the specified HRS limits [**Error! Reference source not found.**].

Based on the irradiated sample measurements [**Error! Reference source not found.**], it is expected that the RRR of Al stabilizer will degrade to the minimum allowed value of 100 in one year of operation. At that point, the magnet will need to be thermo-cycled as the resistivity of Al recovers to its non-irradiated value after warming up to the room temperature [13].
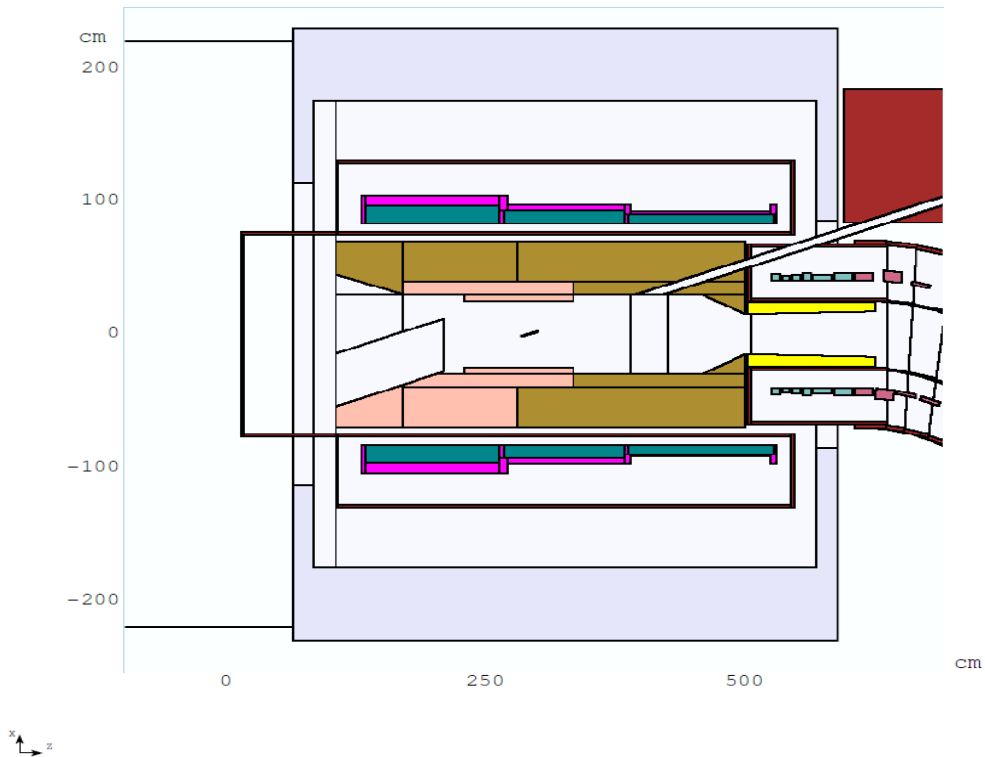

FIGURE 4. MARS15 model cross-section in the horizontal plane with the heat and radiation shield in the warm bore. The HRS consists of high-silicon bronze (brown, 97% Cu+3% Si) and tungsten alloy (pink, 93% W+6.1% Ni+ 0.9% Fe) parts, 45 cm thick in the region around the target.

TABLE 3. Calculated radiation quantities.

Parameter	Unit	Value
Peak absorbed dose	kGy/yr	270
Peak lifetime absorbed dose	MGy	5.4
Peak power density	µW/g	13

Total CM dynamic heat load	W	53
Peak DPA	1/yr	$2.9 \cdot 10^{-5}$

THERMAL ANALYSIS

The radiation heat is extracted from the coil through the system of thermal bridges and plates. Because of the irradiation-induced degradation, one cannot take advantage of thin layers of high-purity Al as it is often done in the conduction-cooled magnets; the thermal bridges and plates need to be sufficiently thick to conduct the heat even after irradiation.

The thermal bridges, made of 1-mm Al sheets of the same composition as the cable stabilizer, are installed between all layers of cables as well as on the inner coil surface and extend throughout each coil length. The ends of the thermal bridges are bent by 90 degrees and glued to the thermal plates through the layers of ground insulation during or after the coil impregnation, as shown in Figure 5. The ground insulation includes three 125 μm layers of dry E-glass with two 25 μm layers of Kapton in between.

The thermal plates, made of 4 mm of high-purity Al, protrude outside of the coil and are welded to the outer surface of the support shell, where the cooling tubes are installed. The ends of the thermal plates are stress-relieved by providing a clearance at the corners of the support shells to accommodate the differential contraction between the coils and shells due to cooling down and Lorentz forces. Layers of mica paper are introduced between the thermal plates, flanges and support shells to avoid accumulation of shear stresses at these interfaces. There is also a layer of high-purity Al installed between the support shells and cooling tubes helping to equalize the thermal loads between the tubes.

The 3D FEM model created within COMSOL Multiphysics code was finalized to the level of individual cable layers and included all the cooling/insulation features described earlier. The simulation was made for the worst case when the RRR of all Al elements (excluding the support structure) was degraded to 100. The law of mixtures was used to define the equivalent thermal conductivities of the insulated cables, the interlayer insulation, and the ground insulation. All other elements had the actual thermal properties of the corresponding materials.

The 3D thermal model of the PS cold mass is shown in Figure 6 together with the dynamic heat load generated by MARS and applied to the cold mass volume. In addition to that, the relevant static heat loads [4] were applied to all external surfaces to model the thermal radiation/gas conduction; to the middle support ring to model the heat load through the axial supports; and to the end flanges to model the heat load through the transverse supports. It was assumed that the cooling tubes are kept at the constant temperature T_0 by the cryogenic system. One half of the cold mass is modeled since the production target lies in the horizontal plane and the heat deposition map is symmetric with respect to that plane.
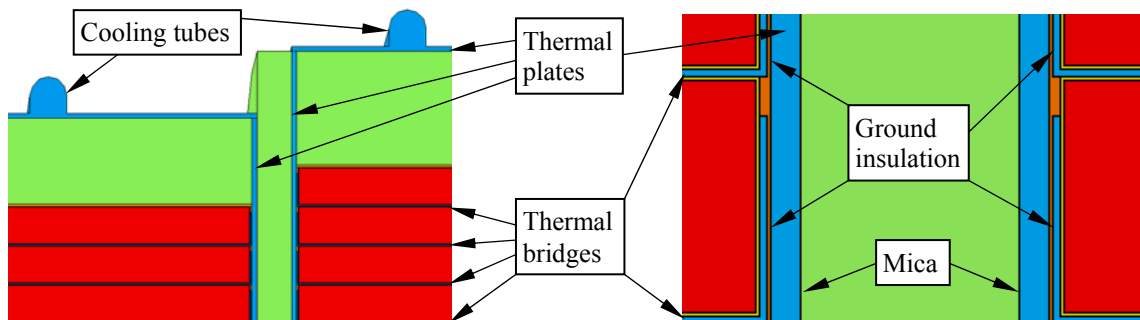

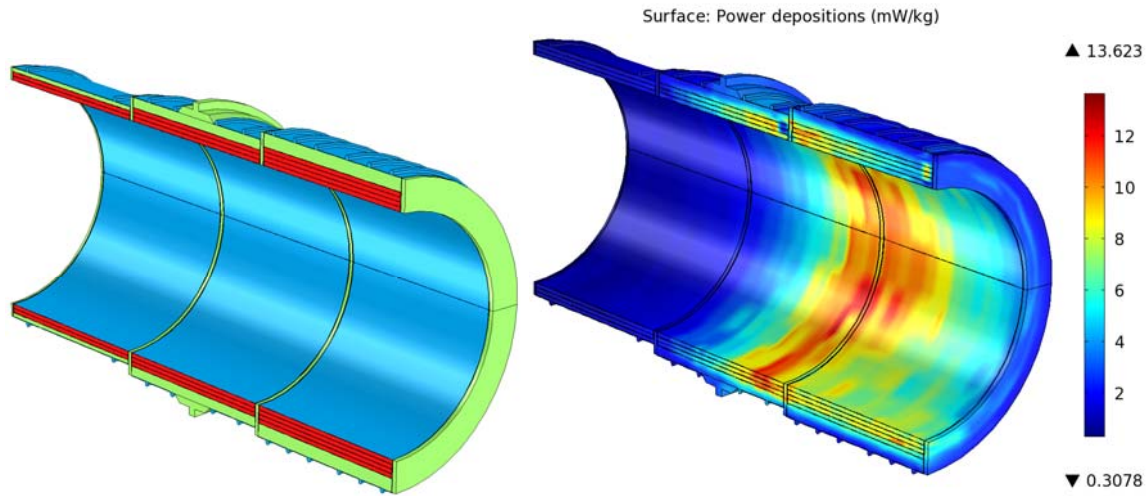**FIGURE 5.** Model cross-section with the view of the coil to coil interface.

FIGURE 6. 3D thermal model (left) and the applied heat depositions (right). The model is rotated by 90 degrees around the magnetic axis for clarity.

The resulting temperature in the cold mass is shown in Figure 7 for $T_0 = 4.6$ K. The maximum temperature is in the middle of the inner surface of the thickest coil; that location coincides with the peak field location, and, therefore directly affects the thermal margin. In order to determine the thermal parameter space, T_0 was varied in 4.2 K – 4.8 K range. Figure 7 shows the peak coil temperature as a function of T_0 for different dynamic power factors representing the scale factor of the dynamic heat load with respect to the nominal.

Under the static heat load, the peak temperature increment between the coil and cooling tubes is only 30 mK, indicating that most of the static heat load is intercepted by the thermal bridges and plates before it enters the coil. Under the nominal dynamic heat load, the temperature increment increases up to ~400 mK. Nevertheless, the peak coil temperature is below the maximum allowable temperature by ~100 mK that provides an additional thermal margin to offset the uncertainly in calculating the power depositions, fabrication tolerances and material properties.
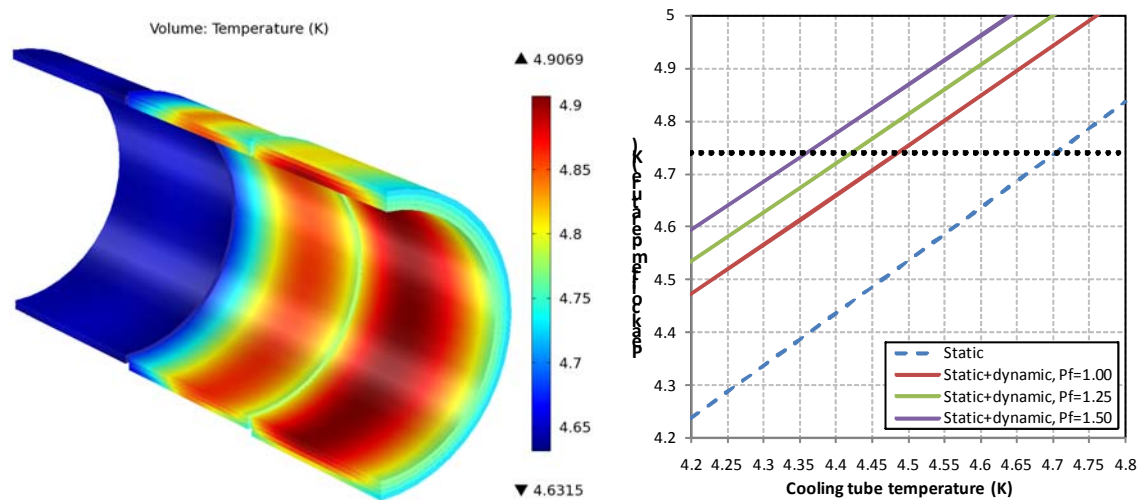

FIGURE 7. Temperature distribution in the coil at T_0=4.6 K under the nominal dynamic heat load (left), and the peak coil temperature vs. the cooling tube temperature for different dynamic power factors (right).

REFERENCES

1. Mu2e CDR: http://mu2e.fnal.gov
2. M. Lamm, "Mu2e Production Solenoid Requirements Document," Mu2e-doc-945.
3. V.V. Kashikhin, et al., "Design Studies of Mu2e Production Solenoid," Mu2e-doc-1110.
4. T. Nicol, et al., "Mu2e Production Solenoid Cryostat Conceptual Design," presented at this conference.
5. A. Yamamoto, T. Kondo, Y. Doi, Y. Makida, K. Tanaka, T. Haruyama, H. Yamaoka, H. ten Kate, L. Bjorset, K. Wada, S. Meguro, J.S.H. ROSS, K.D. Smith, "Design and Development of the ATLAS Central Solenoid Magnet," *IEEE Transactions on Applied Superconductivity*, Vol. 9, No. 2, June 1999, pp.852-855.
6. G. Baccaglioni, B. Blau, G. C. Cartegni, I. L. Horvath, J. Neuenschwander, D. Pedrini, L. Rossi, G. Volpini, "Production and Qualification of 40 km of Al-Stabilized NbTi Cable for the ATLAS Experiment at CERN," *IEEE Transactions on Applied Superconductivity*, Vol. 12, No. 1, March 2002, pp.1215-1218.
7. B. Blau, D. Campi, B. Curé, R. Folch, A. Hervé, I. L. Horvath, F. Kircher, R. Musenich, J. Neuenschwander, P. Riboni, B. Seeber, S. Tavares, S. Sgobba, R. P. Smith, "The CMS Conductor," *IEEE Transactions on Applied Superconductivity*, Vol. 12, No. 1, March 2002, pp.345-348.
8. K. Wada, et al., "Development of High-Strength and High RRR Aluminum-Stabilized Superconductor for the ATLAS Thin Solenoid," *IEEE Transactions on Applied Superconductivity*, Vol. 10, No. 1, March 2000, pp.373-376.
9. A. Yamamoto, et al., "A Thin Superconducting Solenoid Wound With the Internal Winding Method for Colliding Beam Experiments," *Journal de Physics*, C1, 1984, pp.337-340.
10. ATLAS Central Solenoid Technical Design Report, ATLAS TDR-9; CERN/LHCC 97-21, April 1997.
11. MARS code: http://www-ap.fnal.gov/MARS/
12. V.S. Pronskikh, V.V. Kashikhin, N.V. Mokhov, "Radiation and Thermal Analysis of Production Solenoid for Mu2e Experimental Setup," *Proc. of 2011 Particle Accelerator Conference*.
13. J. Popp, R. Coleman, V. Pronskikh, Requirements for the Mu2e Production Solenoid Heat and Radiation Shield, Mu2e-doc-1092.
14. J. A. Horak, T. H. Blewitt, "Isochronal Recovery of Fast Neutron Irradiated Metals," *Journal of Nuclear Materials* **49**, 1973/74, pp.161-180.